This is a preprint, the final version is subject to change, of the American Mineralogist (MSA)
Cite as Authors (Year) Title. American Mineralogist, in press.
(DOI will not work until issue is live.) DOI: http://dx.doi.org/10.2138/am-2017-6178

REVISION 1

Non-destructive, multi-method, internal analysis of multiple inclusions in a single diamond: first occurrence of mackinawite $(Fe,Ni)_{1+x}S$

Giovanna Agrosì [1], Gioacchino Tempesta [1], Daniela Mele [1], Ignazio Allegretta [2], Roberto Terzano[2], Steven B. Shirey [3], Graham D. Pearson [4], Fabrizio Nestola [5]

[1] Dipartimento di Scienze della Terra e Geoambientali, Università degli Studi "Aldo Moro", Via Orabona, 4, 70125 Bari, Italia
[2] Dipartimento di Scienze del suolo, della pianta e degli alimenti (Di.S.S.P.A.), Università degli Studi "Aldo Moro" Via Amendola, 165/A 70126 - Bari – Italia
[3] Department of Terrestrial Magnetism, Carnegie Institution for Science, 5241 Broad Branch Road, NW, Washington, DC 20015, USA
[4] Department of Earth and Atmospheric Sciences, University of Alberta, Edmonton, Alberta Canada T6G 2E3
[5] Dipartimento di Geoscienze, Università degli Studi di Padova, Via G. Gradenigo 6, 35131 Padova, Italia

Abstract

A single gem lithospheric diamond with 5 sulfide inclusions from the Udachnaya kimberlite (Siberia, Russia) has been analyzed non-destructively to track the growth conditions of the diamond. Sulfides are the most abundant mineral inclusions in many lithospheric diamond crystals and are the most favorable minerals to date diamond crystals by Re-Os isotope systematics. Our investigation used non-destructive, micro-techniques, combining X-ray tomography, X-ray fluorescence, X-ray powder diffraction and Raman spectroscopy. This approach allowed us to determine the spatial distribution of the inclusions, their chemical and mineralogical composition on the micro- scale and, finally, the paragenetic association, leaving the diamond host completely unaffected. The sample was also studied by X-ray diffraction topography to characterize the structural defects of the diamond and to obtain genetic information about its growth history. The X-ray topographic images show that the sample investigated exhibits plastic deformation. One set of {111} slip lamellae, corresponding to polysynthetic twinning, affects the entire sample. Chemical data on the inclusions still trapped within the diamond show they are monosulfide solid solutions of Fe, Ni and indicate a peridotitic paragenesis. Micro X-ray diffraction reveals that the inclusions

mainly consist of a polycrystalline aggregate of pentlandite and pyrrothite. A thorough analysis of the Raman data suggests the presence of a further Fe,Ni sulfide, never reported so far in diamonds: mackinawite. The total absence of any oxides in the sulfide assemblage clearly indicates that mackinawite is not simply a "late" alteration of pyrrhotite and pentlandite due to secondary oxidizing fluids entering diamond fractures after the diamond transport to the surface. Instead, it is likely formed as a low-temperature phase that grew in a closed system within the diamond host. It is possible that mackinawite is a more common phase in sulfide assemblages within diamond crystals than has previously been presumed, and that the percentage of mackinawite within a given sulfide assemblage could vary from diamond to diamond and from locality to locality.

Keywords: Diamond, sulfide, mackinawite, non-destructive analyses

Introduction

The study of diamond and mineral inclusions trapped within them may provide critical insights into aspects of deep mantle mineralogy as well as the origin of the cratonic lithosphere and its evolution (Sobolev 1977; Stachel and Harris 2008; Shirey et al. 2013 and references therein). Over the last 30 years (i.e. since Richardson et al. 1984), these studies have also helped to constrain our understanding of the temporal evolution of the lithospheric mantle and the water content of cratonic lithosphere and the Earth's mantle transition zone (Pearson et al. 2014; Novella et al. 2015; Nestola and Smyth 2016; Jean et al. 2016; Taylor et al. 2016). To obtain information about the physico-chemical conditions under which the crystallization of diamond occurred, scientists have mainly investigated the growth history of the diamond crystals, the geochemical and crystallographic features of their inclusions and the relationships between the inclusions and their diamond hosts. These studies have been commonly performed by destructive methods involving crushing (Sobolev et al. 1970; Gurney et al. 1984; Gurney 1989; Aulbach et al. 2009) or ion/laser ablating (Seitz et al.

2003; Gallou et al. 2012) the diamond samples in order to expose the inclusions for conventional geochemical analyses.

Recently the trend has been to cut plates to obtain images of diamond internal growth zoning by cathodoluminescence (Howell et al. 2015 and reference therein). However, in all these approaches, some crucial information about the growth conditions of diamond, such as the entrapment pressure of the inclusions, their original crystallographic orientation with respect to the diamond host (e.g. Nestola et al. 2011; Fedortchouk et al. 2011; Nestola et al. 2012; Nestola 2015; Borges et al. 2016), is lost, or their original volatile content could be lost. In situ investigation of diamond with the inclusions still trapped in it, using non-destructive techniques is the best way to preserve this information. For this reason, in recent years, the scientific community in diamond research has developed a different methodological approach to investigate diamond crystals without destroying the samples. Among different methods, Raman spectroscopy (eg. Sobolev et al. 2000; Pearson et al. 2014; Smith et al. 2016) and quantitative birefringence analysis using the MetriPol™ system (Howell 2012 and references therein) represent the prevalent techniques to measure the elastic effects derived from the differences in thermo-elastic properties between mineral inclusions and host diamond. From measuring these elastic effects, an indication about the entrapment pressure of the inclusions may be obtained and from this the depth (or at least the minimum depth) in the mantle of diamond formation. More recently, non-destructive X-ray diffraction (and micro-X-ray diffraction) analysis (μXRD) was adopted to develop "elastic geobarometry" as a way to determine the depth of crystallization of inclusion-bearing diamonds. Moreover, this technique furnished key information on the diamond-inclusion reciprocal crystallographic orientations useful to constrain protogenesis versus syngenesis (Nestola et al. 2014; Angel et al. 2014; Angel et al. 2015a,b,c; Milani et al. 2016; Nestola et al. 2017).

In this study , with the aim to "map" spatial and chemical information that relate to the origin of the diamond while completely preserving the diamond, we have used a multi-technique approach, adding to the aforementioned micro-Raman spectroscopy and μXRD the following non-destructive

methods: X-ray topography (XRDT), Micro-computed X-ray tomography analysis (μCXRT) and Micro X-ray fluorescence (μXRF). In the past, the capabilities of each of these non-destructive techniques were already experienced in the diamond research, using mainly synchrotron source. μXRF was previously used to obtain direct chemical analysis of inclusions trapped in diamond, providing, in some cases, also 3D reconstruction of maps (e.g. Brenker et al. 2005; Sitepu et al. 2005; Silversmidt 2011; Pearson et al. 2014; La Force et al. 2014). μCXRT has been successfully adopted to locate mineral inclusions in insufficiently transparent diamond crystals (Kovalenko et al. 2012; Nestola et al. 2012; Nimis et al. 2016).

XRDT method, extensively used, in the past, to screen the crystalline quality of natural and synthetic crystals used as electronic devices (Agrosì et al. 2009 and 2011), has been successfully employed in Earth Sciences research to study the growth history of tourmalines, garnets and beryls (Agrosì et al. 2006; Agrosì et al. 2011; Tempesta et al. 2011; Pignatelli et al. 2015). Recently, this method has been applied to provide minerogenetic information on diamond in non-destructive way. The results obtained in two previous studies by XRDT on diamond samples from Finsch mine, South Africa (Agrosì et al. 2013), and from the Udachnaya kimberlite, Siberia (Agrosì et al. 2016), revealed significant petrogenetic relationships between the mineral inclusions and their diamond hosts.

In this study, these techniques were combined, for the first time, to investigate one diamond from Udachnaya kimberlite (Siberia, Russia) with the inclusions still trapped in it, using only conventional sources.

It is worth noting that this methodological approach not only allowed to study the structural defects, define the spatial distribution of the inclusions, determine their chemical composition and identify mineral species, but also allowed to find the first occurrence of mackinawite as an inclusion in diamond. To our knowledge, the only previous suggestion of the possible presence of mackinawite was reported by Thomassot (2006) where an analysis was made of a multi-phase sulfide inclusion within a diamond. However, unfortunately, in this case, the identification of mackinawite was only

made on the basis of chemical analysis and stoichiometry, which alone cannot be used for such a definitive identification. No structural data were reported. So at present, our work reports the first definitive evidence of mackinwaite in diamond.

Experimental methods

Sample

The diamond studied in this work is a brown specimen of type IaAB from Udachnaya kimberlite (Siberia, Russia). The crystal exhibits an octahedral morphology, flattened along the (110) plane, with stepped development of the {111} faces (Fig. 1a). Optical observations revealed that the diamond has anomalous birefringence and contains cleavage planes (CP) and fractures partially healed by dark microinclusions (Fig. 1a). The presence of healed fractures renders it difficult, if not impossible, to observe, using optical microscopy alone, the large included solid phases inside the inner part of diamond.

XRDT

XRDT represents a helpful method to obtain images of extended lattice defects with a resolution limit of a few μm. This method is particularly suitable to study structural defects in diamond because the low attenuation coefficient of the X-ray beam makes this mineral highly transparent to X-rays, allowing investigation of the structural defects of the whole sample, instead of only the surface of sample, as is the case with cathodoluminescence. Indeed, the topographic method used here works in transmission mode and provides images of the strain fields associated with defects, without the necessity to cut the sample in slices.

The topographs, taken with Laue geometry, were carried out using a Rigaku camera with monochromatic radiation ($MoK\alpha_1$) and with a micro-focus X-ray tube. The 1 mm thickness of the sample allows the optimum kinematic diffraction condition $\mu t \approx 1$ (μ = linear absorption coefficient; t = crystal thickness), minimizing X-ray absorption. Spatial resolution using these conditions is about 1-2 μm. Diffraction contrast was recorded on high-resolution photographic films (SR Kodak)

that provide better contrast resolution rather than other recording methods. Characterization of the structural defects was performed by applying the extinction criteria to their diffraction contrasts, according to kinematic and dynamic X-ray diffraction theories (Authier and Zarka 1994). Detailed XRDT procedures used in this study are given in Agrosì et al. (2016).

μCXRT

This technique is a powerful, non-destructive method for obtaining 3D information on internal structures of a large variety of objects (Cnudde and Boone 2013; Howarth et al. 2015). It is able to distinguish highly-X-ray-absorbing mineral inclusions from highly X-ray transparent diamond, providing a 3D reconstruction of the sample and the spatial distribution of the inclusions trapped in it as well as a visualization of their morphologies (see Nestola et al. 2012 for an example of application to diamond).

In this study, the instrument utilized was a SkyScan 1172 microtomograph equipped with a W tube. A 45 kV X-ray source was used with a current of 218 μA. A total of 1200 absorption radiographs were acquired over a 360° rotation with an angular step of 0.3°. Random movement of the vertical axis and multiple-frame averaging to minimize the Poisson noise in the projection images were used. Beam hardening was reduced by the presence of a 0.5 mm Al-filter between source and detector. The nominal spatial resolution for the resulting model was 4.75 μm. The raw data were reconstructed into two-dimensional slice images using the software "NRecon, SkyScan, Belgium". Corrections for the beam-hardening effect and ring artefacts were also applied during the reconstruction process; μCXRT datasets were analyzed using the software "CT-analyser, Skyscan, Belgium".

μXRF

In this study, chemical analyses were obtained by conventional source using an M4 Tornado μXRF (Bruker Nano GmbH, Berlin) equipped with a Rh tube with policapillary optics (50 kV, 600 μA, 30 W) having a spot size of 25 μm. Two XFlash® silicon drift detectors with an active area of 30 mm^2 were used. The resolution was lower than 140 eV for both detectors. For elemental maps, one

spectrum was acquired every 10 μm with both detectors and acquisition time set at 10 ms per pixel. Elemental analyses on inclusions within the diamond were performed with only one detector in order to exclude diffraction peaks which can overlap heavy metal K lines. A live time of 60 s was used. All analyses were performed under vacuum (20 mbar) to avoid Ar absorption and to detect light elements. Spectral quantification was performed in standardless mode using M4 Tornado software. NIST SRM 611 and NIST SRM 613 standards were analyzed in order to periodically test the performance of the instrument.

μXRD

X-ray diffraction measurements were performed using a Rigaku Oxford Diffraction SuperNova single-crystal diffractometer, equipped with a Dectris Pilatus 200K area detector and a Mova X-ray microsource (beam spot ~ 0.12 mm; Nestola et al. 2016). For the measurements, Mo*K*α-radiation, operating at 50 kV and 0.8 mA was used. The sample to detector distance was 68 mm. Data reduction was performed using the CrysAlis software (Rigaku Oxford Diffraction). The instrument is able to perform in "micro powder diffraction mode" to acquire X-ray diffractograms on polycrystalline grains entrapped in diamond crystals with size down to 20-10 μm.

Micro-Raman spectroscopy

Micro-Raman spectroscopy was performed on the sample in backscattered geometry with a Jobin-Yvon Horiba ''XploRATM'' apparatus, equipped with a microscope with 10× and 50× objectives and a motorized x–y stage. The 532 nm line of a class 1 laser used for excitation was coupled with a 1200 line/mm grating and a high-sensitivity CCD air cooled detector with a 1024 pixel. A filter was used to reduce the laser power on the sample. The frequency calibration was performed against the Raman peak of silicon. The instrument allowed a spatial resolution of about 1 μm, with a spectral resolution of 1.8 cm^{-1}. The peak positions were obtained from a multipoint baseline corrected spectrum using the computer program GRAMS/AI 8.0 (Thermo Electron # 2001).

Results

Optical observations reveal that the diamond crystal, although transparent, contains several microfractures healed by dark and opaque material making difficult the optical study of the inclusions (Fig. 1a). The crystal exhibits anomalous birefringence and a trace of cleavage parallel to the (111) plane passing through the whole crystal (Fig. 1a, 1b, 1c).

In order to visualise the inclusions, the crystal was studied by μCXRT. The inclusions could be easily distinguished from the host diamond crystal by simply thresholding the grey value histogram of the reconstructed images (Fig. 1b).

3D tomographic surface rendering (see Fig. 1b) shows five highly absorbing large inclusions on the core of the diamond. Three of the inclusions that extend near the cleavage trace exhibit an apparent diamond-imposed morphology, whereas two other inclusions show irregular, polyhedral morphologies. Some cracks propagating through the diamond from each of the inclusions may be ascribed to their different thermo-elastic behaviour with respect to the diamond host. Some healed fractures, optically observed, do not cause any contrasts in the tomographic images. Only one healed fracture, labelled F, in the lower part of the figure can be observed (Fig. 1b). The tomographic study reveals no connection between this fracture and the inclusions and consequently, it is not related to the trapped inclusions.

The X-ray topographic images (Fig. 1c and Fig. 2) show that the diamond exhibits micro-laminations (μL) parallel to the (111) plane (Fig. 1c and Fig. 2a, 2c). Such laminations represent the polysynthetic twinning of micro-lamellae commonly found in diamond crystals (Titkov et al. 2012). The diffraction contrasts observed in these images reveal regions slightly disoriented relative to one another. Indeed, in Figure 2 it can be observed that under the same diffraction vector, and thus under the same Bragg angle, it is necessary to place the diamond in two different positions differing by a few arc-seconds to obtain the diffraction of the whole sample. In Figure 2d the diffraction contrast corresponding to the diamond core can be observed (see the dashed red line). In the core, corresponding to early stage of diamond crystal growth, the large inclusions are out of contrast. The topographic images show, additionally, that the fracture previously observed by optical microscopy

and by X-ray tomography and labelled as cleavage plane, forms an angle of about 70 degrees with respect to the direction of the microlaminations. This confirms that this discontinuity coincides with a typical octahedral cleavage along the (1-11) plane. It is worth noting that the cleavage plane misaligns the microlaminations and thus it is post-twinning feature.

The chemical composition of the inclusions was detected by μXRF. Semi-quantitative chemical analyses obtained on the large inclusions (Table 1) suggest that these inclusions are essentially an aggregate of Fe,Ni sulfides with small amounts of Cu and Cr. Due to the microcrystalline nature of the aggregate (see micro X-ray diffraction results) and the relatively large beam diameter (about 25 μm), it was not possible to obtain a reliable chemical composition for each of the three identified sulfides at the 1-2 μm scale. However, we were able to obtain a bulk chemical composition that corresponds with a formula: $(Fe_{0.83}Ni_{0.31}Cu_{0.01}Cr_{0.01})_{\Sigma 1.16}S$.

Chemical maps obtained on the whole sample were compared with a μCXRT image (Fig. 3). To verify the consistency between the chemical maps and the contrast observed by micro-tomography, an image showing the same inclination of the sample observed on the maps was obtained from the μCXRT reconstruction. The sample shape visible from the maps is deformed due to the instrument geometry; the [110] axis appears to be inclined with respect to the images shown in Figures 1 and 2, where the sample is placed exactly perpendicular to the [110] direction. The correlation between the μ-XRF images and the properly oriented tomographic image confirms the content of Fe, Ni and Cu in the inclusions and reveals that the aforementioned inclination produces the following artefacts: inclusions 2 and 3 appear to be overlapping and the fracture F appears connected to these inclusions (Fig. 3). Moreover, the maps reveal that the contrast of this fracture observed on the tomographic images is due to a secondary filling of a Fe-rich material.

No additional information about the nature of the dark phases that healed the other fractures could be acquired. The lack of tomographic contrast and the chemical information corresponding to these

239 secondary microinclusions could be due to the fact that they are likely dominated by light elements,
240 as well as carbon, decorating the pathways of late stage fluids.
241 The mineralogical composition of the inclusions was established by means of μXRD and micro-
242 Raman spectroscopy. The X-ray diffractogram (Figure 4) confirms that the inclusions mainly
243 consist of a microcrystalline aggregate of Fe-Ni sulfides (no diffraction spots, typical of single
244 crystal, were found during the measurements). In detail, the main peaks were ascribed to pentlandite
245 and pyrrhotite (Fig. 4). However, the Raman results (see below) indicate the presence of a third
246 sulphide, mackinawite. Unfortunately, the diffraction peaks of mackinawite are totally overlapped
247 with those of pentlandite and thus it is not trivial to definitively confirm its presence solely by
248 diffraction. Using the software HighScore Plus ^{TM} (Panalytical), we attempted to obtain a phase
249 quantification of the three sulfides (a reference pattern of mackinawite was added to the
250 diffractogram based on the Raman results). Considering that the most intense diffraction peak of
251 mackinawite is the 001 at about 5.05 Å (Figure 4), it is evident that such a phase would represent a
252 very minor fraction of the aggregate. In detail, as visible in the pie graph in Figure 4, we obtained:
253 pyrrhotite = 54%, pentlandite = 44% and mackinawite = 2% (the reference codes from the ICSD
254 database are: 98-000-5868 for pyrrhotite, 98-001-7595 for pentlandite and 98-004-8846 for
255 mackinawite).
256 Micro-Raman spectroscopy confirms clearly the presence of mackinawite. Actually, if the x-ray
257 diagrams of mackinawite, pentlandite and pyrrhotite show a number of overlapped peaks, the
258 corresponding Raman spectra are very different (Figure 5a). In Figure 5b, we show four spectra
259 taken on the inclusions, which were compared to the Raman Ruff database (Lafuente et al. 2015),
260 obtaining a very satisfactory match with mackinawite (ID: R060388), a sulphide of Fe and Ni, with
261 reported chemical formula $(Fe,Ni)_{1.00\text{-}1.07}S$. Nevertheless, a further comparison carried out between
262 our spectra and other literature spectra measured on natural and synthetic mackinawite (Boughriet
263 et al. 1997; Bourdoiseau et al. 2008; Genchev et al. 2016; and Hansson et al. 2006) definitively
264 confirms the presence of mackinawite trapped in the diamond investigated here.

Discussion

Structural defects

The diamond studied exhibits micro-laminations that correspond to polysynthetic twinning. The development of one system of micro-lamellae along the whole sample confirms that the diamond is a single crystal and not an aggregate of different grains, as indicated also by the morphological evidence. The micro-lamellae are likely formed by slip-plane development, dislocation generation and motion during plastic deformation and correspond to {111} micro-twins (De Vries 1975; Shiryaev et al. 2007; Titkov et al. 2012; Gainutdinov et al. 2013). These kinds of defects were commonly related to the brown and pink colour of diamond crystals even though the same features were recently found also in a colorless IaAB diamond from Finsch mine (South Africa; Agrosì et al. 2013) and, conversely, not found in some pink diamond samples (Howell et al. 2015). The formation of the twinned micro-lamellae is an important mechanism for deformation accommodation in diamond and represents the first step of the process. Such accommodation occurs by means of significant rearrangements of point defects as impurities, vacancies and carbon interstitials between the twin planes under applied stress and by <110> {111} dislocation glide (Tkach and Vishnevsky 2004; Gaillou et al. 2010).

The quantitative estimation of the mechanical conditions under which micro-twinning occurs is very difficult to determine. Previous high-pressure and high-temperature experiments performed on synthetic diamonds in order to evaluate the mechanisms of deformation under confined pressure showed that {111} micro-twins begin to form at $T \geq 1000$°C and P = 3.5 GPa for polycrystalline diamond crystals (Yu et al. 2012) and $T \geq 1700$ °C and P = 5.1 GPa for single crystals (Howell et al. 2012). However, it is worth noting that during the last experiment, the temperature was enhanced to obtain shorter durations for the experiments (such temperature is significantly above the typical temperature at the base of the lithosphere, being about 1350 °C; see Mather et al. 2011). Moreover, in our case, these T/P values should be considered only approximate because the mechanism of

plastic deformation in natural diamond crystals also depends on the contribution of crystalline growth defects, which are the major factors affecting material's strength. Unfortunately, it is very difficult to re-establish the early state of crystalline defects in plastically deformed natural diamond crystals. Nevertheless, even if the HP-HT experiments carried out on synthetic diamond samples cannot indicate specific values of stress/strain for natural diamond crystals, at least they suggest that the plastic deformation of our diamond occurred under a typical range of P and T conditions for the upper mantle and are not related to the late stage of diamond ascent.

Inclusions still trapped within diamond

The analysis of the inclusions still trapped within the diamond focused on 5 large inclusions located in the core, that represent the early stage of diamond growth. The micro-tomography reconstruction reveals clear diamond-imposed morphology for at least three inclusions, whereas two of them appear to have irregular shapes. Unfortunately, the post growth plastic deformation masks any information about the entrapment mechanism of inclusions.

Chemical analyses of these aggregates reveal that they are Fe-Ni sulfides with small amounts of Cu and Cr. The results obtained allow us to assign the paragenetic suite to this diamond: the mean content of Cr ($\geq$ 0.19 wt%) and Ni ($\geq$ 18wt%) (Table 1), in agreement with literature data, indicate a peridotitic origin (Stachel and Harris 2008; Taylor and Liu 2009; Thomassot et al. 2009). As we mentioned above, non-destructive analyses by X-ray diffraction and micro-Raman spectroscopy allowed us to identify the sulfide assemblage, consisting of pyrrhotite, pentlandite and mackinawite. Sulfides are the most dominant mineral class residing as inclusions within diamonds world-wide (e.g. Gurney et al. 1979; Stachel and Harris 2008). It is generally accepted that diamond can crystallize from metasomatic C-H-N-O-S fluids, carbonatitic fluids (Haggerty 1986; Westerlund et al. 2004; Thomassot et al. 2007, Thomassot et al. 2009; Aulbach et al. 2009), from a melt, or under sub-solidus conditions (Stachel and Luth 2015). Experimental data applied to mantle-derived diamond genesis demonstrates that sulfide melts with dissolved carbon are capable of forming a

316 limited mass of diamond crystals with specific mineralogical and physical properties (Shuskanova
317 and Litvin 2008).
318 It is generally agreed that sulfide inclusions are encapsulated as a monosulfide solid solution in the
319 Fe-Ni-S system, with a minor amount of Cu. The different thermal expansion properties of mono-
320 sulfides and diamond creates a series of cracks radiating from the sulfides after encapsulation.
321 During cooling, the monosulfide solid solution become unstable and exsolution to a fine-grained
322 intergrowth of pyrrhotite, pentlandite, chalcopyrite and sometimes pyrite, occur. Chalcopyrite,
323 especially, migrates into the minute cracks in the diamond crystals (Taylor and Liu 2009). A
324 protogenetic origin has been invoked for the origin of sulfide inclusions in the diamond by Spetsius
325 et al. (2002), Thomassot et al. (2009) and Jacob et al. (2016) while Wiggers De Vries et al. (2013)
326 provided evidence for a co-genetic nature.
327 Recently, Bataleva et al. (2016) synthesized diamond crystals, in the SiO2-(Mg,Ca)CO3-(Fe,Ni)S
328 system at 321 6.3 GPa and ~ 1700{degree sign}C, and obtained stones with a wide variety of
329 syngenetic inclusions, including quenched sulphide melt with elongated “bottle” or “bullet” shapes.
330 The shape of the inclusions found in this study do not match with the Bataleva et al. (2016) sulfide
331 morphologies, suggesting a different origin. The faceted morphology could be ascribed to a
332 protogenetic origin, even if we have insufficient experimental evidence to determine definitively
333 whether our inclusions are syngenetic or protogenetic. Indeed, the results obtained by XRDT clearly
334 indicate that the studied inclusions were trapped in the early stage of diamond growth.
335 **Mackinawite**
336 A further important discovery of our work is the presence of mackinawite in the sulfide assemblage.
337 This phase represents a metastable tetragonal iron sulfide and was formally defined as a mineral by
338 Evans et al. (1964) from the Mackinaw Mine, Washington. Previously, Kuovo et al. (1963) had
339 described a tetragonal iron sulfide from the Outokumpu Mine, Finland. In both of these
340 occurrences, mackinawite was associated with a high temperature phase assemblage apparently
341 related to the monosulfide-solid solution. Subsequently, mackinawite has been found commonly in

342 other high temperature mineral associations (Rickard et al. 2006 and references therein) as well as
343 in serpentinized ultramafic rocks or in low-temperature aqueous systems, associated with pyrrhotite,
344 pentlandite, cubanite and chalcopyrite (Ostwald 1978; Lennie et al. 1995; Wolthers et al. 2005).
345 Mackinawite has also been occasionally found in iron and carbonaceous chondrite meteorites
346 (Buchwald 1977). To date, the compositional range and stability of this sulfide are not fully
347 established. Bishop et al. (1975), in a review on sulfides from a spinel Lherzolite from the De Beers
348 pool mines, ascribed mackinawite formation to two different mechanisms operating at low
349 temperature: (a) an initial late-stage replacement of pentlandite and subsequently (b) exsolution
350 producing an intergrowth of lamellae of different Fe/Ni sulfides.
351 Previous studies of mackinawite stability in highly reducing and anoxic low temperature
352 environments report the phase as a low-temperature precursor of pyrite, greigite, valleriite and in
353 some cases marcasite at temperatures < 300°C (Schoonen and Barnes 199la, 1991b, 199lc; Lennie
354 et al. 1995; Wolthers st al. 2003; Rickard et al. 2006; Li et al. 2008; Wang et al. 2015). These
355 studies also investigated the thermal stability of mackinawite reporting that on heating synthetic
356 mackinawite an irreversible transition to hexagonal pyrrhotite occurred in the temperature range of
357 120°-200°C. Additionally, Csákberényi-Malasics et al. (2012) established that mackinawite was the
358 first phase to crystallize from the amorphous Fe monosulfide in aqueous solutions at ambient
359 temperatures and pressures. In the same anaerobic environment, the formation of mackinawite was
360 recently attributed also to the activities of prokaryotes (Rickard et al, 2017). Despite these numerous
361 studies, the thermal stability of mackinawite containing significant amounts of Co, Ni, or Cu, and
362 its role in the exsolution mechanism of monosulfide solid solution are not satisfactorily known
363 especially with regard to the pressure/temperature history of the diamond host during crystallization
364 and sampling+transport in the kimberlite eruption.
365 The finding of mackinawite trapped in diamond in this study allows for two different hypotheses: it
366 is either of secondary origin or it is primary. In the first case, a metasomatic fluid could have
367 penetrated along the fractures generating a replacement of the phases trapped initially. This

hypothesis is rejected because it would be unusual that such a secondary replacement would have produced only mackinawite with no other associated phases like djerfisherite, hematite, magnetite, ilmenite (Sharygin et al. 2003) or others phases commonly found in altered Fe/Ni sulfides. None of these phases are observed. The second hypothesis proposes a primary origin of the mackinawite. This hypothesis is supported by the texture of the sulphide inclusion. The presence of pentlandite and pyrrhotite in a very small assemblage with mackinawite suggests a typical exsolution process from a monosulfide melt. Mackinawite could be formed during the later stages of the exsolution process.

Mackinawite is very difficult to identify when it belongs to a complex intergrowth of pyrrhotite and pentlandite. During routine chemical analyses performed on sulfides released from diamond samples it would be practically impossible to find the mineral, especially if it is present in very low concentrations, as observed here. The extraction of inclusions is usually carried out by crushing and polishing diamond crystals or by their combustion. All of these processes may contribute to the presence of very small amounts of mackinawite being destroyed or over-looked.

To determine exactly the phases exsolved from mono-sulphide solid solution it would be necessary to know some crucial factors such as the bulk starting composition (e.g., the Ni content), the cooling history, pressure and the kinetics of the exsolution process.

The presence of "primary" mackinawite in a sulfide assemblage within a diamond raises further possibilities for the fractionation of Re from Os and hence the development of complex Re-Os isotope systematics during the cooling and exsolution of sulfides included in diamonds. The precise dating sulfides within diamond (Pearson et al. 1998) requires the full recovery of all sulfide phases associated with an exsolved sulfide aggregate (e.g., Richardson et al. 2001), to minimise experimental "error" in the measurement of the Re/Os ratio.

While we do not know the systematic partitioning behaviour of Re and Os between mackinawite and other sulfides in detail, it will likely fractionate Re from Os differently from other co-existing sulfide phases. ~~and~~ H~~h~~ence it means that it is critical, if applying Re-Os geochronology to sulfide

394 grains, to recover the entire sulfide for analysis, otherwise the Re/Os system will not be accurately
395 analysed. This further emphasises the need for great care in recovering as much of the sulfide as
396 possible in Re-Os geochronology and highlights the very significant problems encountered when
397 using laser-ablation analysis for diamond sulfide Re-Os geochronology, because this method uses
398 polished sulfides where always some portion of the sulfide has been lost.
399

400 **Implications**

401 Sulfides represent the most abundant mineral inclusions in lithospheric diamond crystals (Stachel
402 and Harris 2008). They cover a key role in determining (a) the paragenesis of their diamond hosts as
403 well as (b) their age by Re-Os systematics. In order to avoid serious mistakes in both (a) and (b) it is
404 evident that the chemical system must remain uncorrupted since the time of the diamond formation.
405 Our non-destructive multi-analytical approach definitively shows a reliable experimental protocol to
406 study sulfides still trapped within diamond preserving the "entirety" of inclusions. The set of
407 different methods used in this study reports the presence of small amount of mackinawite as part of
408 the typical polycrystalline aggregate of pentlandite and pyrrothite found as inclusion within a
409 diamond. Although this is the first report of mackinawite as inclusion in diamond, we consider such
410 sulfide not so rare as it is likely that previous works focused on sulfides could have overlooked it.
411 Actually, the possibility that mackinawite is a more common phase in sulfide assemblages within
412 diamond than previously presumed, and that the percentage of mackinawite within a given sulfide
413 assemblage could vary from diamond to diamond and from locality to locality, cannot be ruled out.
414 The genetic implications of the presence of such new sulfide within a diamond as a primary phase
415 could have some influences in the Re-Os fractionation and, in turn, in the diamond dating. This
416 study provides evidence to address correctly future studies on sulfide inclusions in diamond and
417 could open new scenarios on the thermal evolution of the diamond host.

418
419

Acknowledgements

The authors are very grateful to National Project PONa3_00369 "SISTEMA" and to Laboratories network "Micro X-ray Lab" of the University of Bari "A. Moro" for the analyses by micro-CT and micro-XRF, respectively. The research was supported by ERC Starting Grant INDIMEDEA (grant number 307322) awarded to Fabrizio Nestola, University of Padova (Italy).

References cited

Agrosì, G., Bosi, F., Lucchesi, S., Melchiorre, G. and Scandale, E. (2006) Mn-tourmaline crystals from island of Elba (Italy): growth history and growth marks. American Mineralogist, 91, 944-952.

Agrosì, G., Capitani, G. C., Scandale, E. and Tempesta, G. (2011) Near-atomic images of interfaces between twin-related lamellae in a synthetic 6H-SiC sample. Physics and chemistry of minerals, 38 (2), 101-109. Doi: 10.1007/s00269-010-0387-y

Agrosì, G., Nestola F., Tempesta G., Bruno M., Scandale, E. and Harris, J.W. (2016) X-ray topographic study of a diamond from Udachnaya: Implications for the genetic nature of inclusions. Lithos, 248 (25), 153–159.

Agrosì, G., Scandale, E. and Tempesta, G. (2011) Growth marks of titanian-andradite crystals from Colli Albani (Italy). Periodico Di Mineralogia, 80, 89–104.

Agrosì, G., Tempesta, G., Scandale, E. and Harris, J.W. (2013) Growth and post-growth defects of a diamond from Finsch mine (South Africa). European Journal of Mineralogy, 25 (4), 551-559.

Agrosì, G., Tempesta, G., Capitani, G.C., Scandale, E. and Siche, D. (2009) Multi-analytical study of syntactic coalescence of polytypes in a 6H–SiC sample. Journal of Crystal Growth, 311, 4784–4790.

Angel, R.J., Mazzucchelli, M.L., Alvaro, M., Nimis, P., and Nestola, F. (2014) Geobarometry from host-inclusion systems: The role of elastic relaxation. American Mineralogist, 99, 2146–2149.

Angel, R.J., Milani, S., Alvaro, M., and Nestola, F. (2015a). OrientXplot: a program to analyse and display relative crystal orientations. Journal of Applied Crystallography, 48.

---, R.J., Nestola, F., and Mazzucchelli, M.L. (2015b) Diamond thermoelastic properties and implications for determining the pressure of formation of diamond inclusion systems. Russian Geology and Geophysics, 56, 225–234.

---, R.J., Nimis, P., Mazzucchelli, M.L., Alvaro, M., and Nestola, F. (2015c) How large are departures from lithostatic pressure? Constraints from host–inclusion elasticity. Journal of Metamorphic Geology, 33, 801–813.

Aulbach, S., Stachel, T., Creaser, R. A., Heaman, L. M., Shirey, S. B., Muehlenbachs, K., Eichenberg, D. and Harris, J. W. (2009) Sulphide survival and diamond genesis during formation and evolution of Archaean subcontinental lithosphere: A comparison between the Slave and Kaapvaal cratons. Lithos, 112S, 747–757.

Authier, A. and Zarka, A. (1994) X-ray topographic study of the real structure of minerals, in A.S. Marfunin (Ed.), Composition, Structure and Properties of Mineral Matter. Springer -Verlag, Berlin, p. 221-233.

Bataleva, Y.V., Palyanov, N. Y., Borzdov, Y. M., Kupriyanov, I. N. and Sokol, A. G. (2016) Synthesis of diamonds with mineral, fluid and melt inclusions. Lithos, 265, 292–303.

Bishop, F.C., Smith, J.V. and Dawson, J.B. (1975) Pentlandite-magnetite intergrowth in De Beers spinel Lherzolite: review of sulfide in nodules. Physics and Chemistry of the Earth, 9, 323-337.

Borges, M.P.A.C., Moura, M.A., Lenharo, S.L.R., Smith , C.B. and Araujo, D.P. (2016) Mineralogical characterization of diamonds from Roosevelt Indigenous Reserve, Brazil, using non-destructive methods. Lithos, 265, 182–198.

Boughriet, A., Figueiredo, R., Laureyns, J. and Recourt, P. (1997) Identification of newly generated iron phases in recent anoxic sediments: 57Fe Mossbauer and microRaman spectroscopic studies. Journal of Chemical Society Faraday Transactions 93, 3209-3215.

Bourdoiseau, J. A., Jeannin, M., Sabot, R., Remazeilles, C. and Refait, P. (2008) Characterisation of mackinawite by Raman spectroscopy: Effects of crystallisation, drying and oxidation. Corrososion Science, 50, 3247-3255. doi.org/10.1016/j.corsci.2008.08.041

Brenker, F. E., Vincze, L., Vekemans, B., Nasdala, L., Stachel, T., Vollmer, C., Kersten, M., Somogyi, A., Adams, F., Joswig, W. and Harris, J.W. (2005) Detection of a Ca-rich lithology in the Earth's deep (>300 km) convecting mantle. Earth and Planetary Science Letters, 236, issue 3-4, 579-587.

Buchwald, V.F. (1977) The mineralogy of iron meteorites. Philosophical Transactions of the Royal Society. London, A. 286, p. 453–491.

Cnudde, V. and Boone, M.N. (2013) High-resolution X-ray Computed Tomography in Geosciences: a Review of the Current Technology and Applications. Earth-science Reviews, 123, 1–17.

Csákberényi-Malasics D., Rodriguez-Blanco, J. D., Kovács Kis V., Rečnik, A., Benning, L. G. and Pósfai, M. (2012) Structural properties and transformations of precipitated FeS. Chemical Geology, 294-295, 249–258.

De Vries, R.C. (1975) Plastic deformation and ‘‘work-hardening’’ of diamond. Materials Research Bulletin, 10, 1193–1200.

Evans, H. T., Milton, C., Chao, E. C. T., Adler, I., Mead, C., Ingram, B. and Berner, R. A. (1964) Valleriite and the new iron sulfide, mackinawite, U.S. Geological Survey Professional Paper, 475-D, 64-69.

Fedortchouk, Y., Manghnani, M.H., Hushur, A., Shiryaev, A., and Nestola, F. (2011) An atomic force microscopy study of diamond dissolution features: The effect of H2O and CO2 in the fluid on diamond morphology. American Mineralogist, 96, 1768–1775.

Gaillou, E., Post, J.E., Bassim, N.D., Zaitsev, A.M., Rose, T., Fries, M.D., Stroud, R.M. and Butler, J.E. (2010) Spectroscopic and microscopic characterizations of color lamellae in natural pink diamonds. Diamond and Related Materials, 19 (10), 1207-1220.

Gaillou, E., Post, J.E., Rose, T. and Butler, J.E. (2012) Cathodoluminescence of natural, plastically deformed pink diamonds Microscopy and Microanalysis, 18 (6), 1292-1302.

Gainutdinov, R.V., Shiryaev, A.A., Boyko, V.S. and Fedortchouk, Y. (2013) Extended defects in natural diamonds: An Atomic Force Microscopy investigation. Diamond and Related Materials, 40, 17-23.

Genchev, G. and Erbe, A. (2016) Raman Spectroscopy of Mackinawite FeS in anodic iron sulfide corrosion Products. Journal of The Electrochemical Society, 163 (6) C333-C338.

Gurney, J.J. (1989) Diamonds. In J. Ross, Ed., Kimberlite and Related Rocks: Their Mantle/Crust Setting, Diamonds, and Diamonds Exploration. Geological Society of Australia Special Publication, 14, 935-965.

Gurney, J.J., Harris, J.W., and Richardson, R.S. (1979) Silicate and oxide inclusions in diamonds from the Finsch kimberlite pipe. In F.R. Boyd and H.O.A. Meyer, Eds. Kimberlites,

513 diatremes, and diamonds: Their geology, petrology, and geochemistry, p. 1-15. American
514 Geophysical Union, Washington, D.C.

515 Gurney, J.J., Harris, J.W. and Rickard, R.S. (1984) Silicate and oxide inclusions in diamonds from
516 the Orapa mine, Botswana. Kimberlites II: The Mantle and Crust-Mantle Relationships, p.
517 3-9

518 Haggerty, S. E. (1986) Diamond genesis in a multiply constrained model. Nature, 320, 34-38.

519 Hansson, E. B., Odziemkowski, M. S. and Gillham, R. W. (2006) Formation of poorly crystalline
520 iron monosulfides: Surface redox reactions on high purity iron, spectroelectrochemical
521 studies. Corrosion Science, 48, 3767.

522 Howell, D. (2012) Strain-induced birefringence in natural diamond: a review. European Journal of
523 Mineralogy, 24, 575–585.

524 Howell, D., Piazolo, S., Dobson, D.P., Wood, I.G., Jones A.P., Walte, N., Frost, D.J., Fisher, D.,
525 Griffin, W.L. (2012) Quantitative characterization of plastic deformation of single diamond
526 crystals: A high pressure high temperature (HPHT) experimental deformation study
527 combined with electron backscatter diffraction (EBSD) Diamond & Related Materials, 30,
528 20–30.

529 Howell, D., Fisher, D., Piazolo S., Griffin W.L. and Sibley, S. J. (2015) Pink color in Type I
530 diamonds: Is deformation twinning the cause? American Mineralogist, 100, 1518–1527.

531 Howarth, G.H., Sobolev, N.V., Pernet-Fisher, J.F., Ketcham, R.A., Maisano, J.A., Pokhilenko,
532 L.N., Taylor, D. and Taylor, L.A. (2015) 3-D X-ray tomography of diamondiferous mantle
533 eclogite xenoliths, Siberia: A review. Journal of Asian Earth Sciences, 101, 39-67.

534 Jacob, D. E., Piazolo, S., Schreiber, A. and Trimby, P. (2016) Redox-freezing and nucleation of
535 diamond via magnetite formation in the Earth's mantle. Nature Communications, 7, 11891
536 DOI: 10.1038/ncomms11891

537 Jean, M.M., Taylor, L.A., Howarth, G.H., Peslier, A.H., Fedele, L., Bodnar, R.J., Guan, Y., Doucet,
538 L.S., Ionov, D.A., Logvinova, A.M., Golovin, A.V. and Sobolev, N.V.(2016) Olivine
539 inclusions in Siberian diamonds and mantle xenoliths: Contrasting water and trace-element
540 contents. Lithos, 265, 31-41.

Kovalenko, A., Petráková, V., Ashcheulov, P., Záliš S., Nesládek, M., Kraus, I. and Kratochvílová, I. (2012) Parameters affecting the luminescence of nanodiamond particles: quantum chemical calculations. Physica Status Solidi, A 209, 1769-1773.

Kouvo, O., Yrjo, V. and Long, J.V.P. (1963) A tetragonal iron sulfide. American Mineralogist, 48, 511-524.

La Force, B., Schmitz, S., Vekemans, B., Rudloff, J., Garrevoet, J., Tucoulou, R., Brenker, F., Martinez-Criado and G., Vincze L. (2014) Nanoscopic X-ray Fluorescence imaging of meteoritic particles and diamond inclusions. Analytical Chemistry, 86, 12369-12374. doi.org/10.1021/ac503764h

Lafuente, B., Downs, R.T., Yang, H., and Stone, N. (2015) The power of databases: the RRUFF project. In: Highlights in Mineralogical Crystallography, T Armbruster and R M Danisi, eds. Berlin, Germany, W. De Gruyter, p. 1-30.

Lennie, A.R., England, K.E.R. and Vaughan, D.J. (1995) Transformation of synthetic mackinawite to hexagonal pyrrhotite: A kinetic study. American Mineralogist, 80, 960-967.

Li, Y., van Santen, R.A. and Webe, Th. (2008) High-temperature FeS–FeS2 solid-state transitions: Reactions of solid mackinawite with gaseous H2S. Journal of Solid State Chemistry, 181, 3151–3162.

Mather, K.A., Pearson, D.G., McKenzie, D., Kjarsgaard, B. and Priestley, K. (2011) Constraining the depth and the thermal history of cratonic lithosphere using peridotite xenolith and xenocryst thermobarometry and seismology. Lithos, 125, 729-742.

Milani S., Nestola F., Angel R.J., Nimis P. and Harris J.W. (2016) Crystallographic orientations of olivine inclusions in diamonds. Lithos, 265, 312-316.

Nestola F. and Smyth J.R. (2016) Diamonds and water in the deep Earth: a new scenario. International Geology Review, 58, 3, 263-276.

Nestola, F., 2015. The crucial role of crystallography in diamond research. Rendiconti Lincei, 26, 225-233.

Nestola, F., Merli, M., Nimis, P., Parisatto, M., Kopylova, M., Stefano, A. De, Longo, M., Ziberna, L., and Manghnani, M. (2012a) In situ analysis of garnet inclusion in diamond using single-crystal X-ray diffraction and X-ray micro-tomography. European Journal of Mineralogy, 24, 599–606.

571 ---, F., Nimis, P. and Angel, R.J. (2012b) Diamonds, the mantle petrologist's best friends. European
572 Journal of Mineralogy, 24, 561–562.

573 Nestola, F., Nimis, P., Ziberna, L., Longo, M., Marzoli, A., Harris, J.W., Manghnani, M.H., and
574 Fedortchouk, Y. (2011) First crystal-structure determination of olivine in diamond:
575 Composition and implications for provenance in the Earth's mantle. Earth and Planetary
576 Science Letters, 305, 249–255.

577 Nestola, F., Jung H. and Taylor, L. A. (2017) Mineral inclusions in diamonds may be synchronous
578 but not syngenetic. Nature Communications, 8, 14168 doi: 10.1038/ncomms14168

579 Nestola, F., Burnham, A.D., Peruzzo, L., Tauro, L., Alvaro, M., Walter, M.J., Gunter, M., Anzolini,
580 C. and Kohn, S.C. (2016) Tetragonal Almandine-Pyrope Phase, TAPP: finally a name for it,
581 the new mineral jeffbenite. Mineralogical Magazine, 80, 1219-1232.

582 Nimis, P., Alvaro, M., Nestola, F., Angel, R. J., Marquardt, K., Rustioni, G., Harris, J. W. and
583 Marone, F. (2016) First evidence of hydrous silicic fluid films around solid inclusions in
584 gem-quality diamonds. Lithos, 260, 384-389.

585 Novella, D., Bolfan-Casanova, N., Nestola, F. and Harris, J.W. (2015) H_2O in olivine and garnet
586 inclusions still trapped in diamonds from the Siberian craton: Implications for the water
587 content of cratonic lithosphere peridotites. Lithos, 230, 180-183.

588 Ostwald, J. (1978) A note on the occurrences of nickeliferous and cupriferous mackinawite.
589 Mineralogical Magazine, 42, 516–517.

590 Pearson, D. G., Shirey, S. B., Harris, J. W., and Carlson, R. W. (1998) A Re-Os isotope study of
591 sulfide diamond inclusions from the Koffiefontein kimberlite, S.Africa: constraints on
592 diamond crystallisation ages and mantle Re-Os systematics: Earth Planetary Science Letters,
593 160, 311-326.

594 Pearson, D.G., Brenker, F.E., Nestola, F., McNeill, J., Nasdala, L., Hutchison, M.T., Matveev, S.,
595 Mather, K., Silversmit, G., Schmitz, S., Vekemans, B. and Vincze, L. (2014) Hydrous
596 mantle transition zone indicated by ringwoodite included within diamond. Nature, 13,
597 507(7491), 221-224.

598 Pignatelli, I., Giuliani, G., Ohnenstetter, D., Agrosì, G., Mathieu, S., Morlot, C. and Branquet, Y.
599 (2015) Colombian trapiche emeralds: recent advances in understanding their formation.
600 Gems and Gemology, 51 (3), 222-259.

601 Richardson S. H., Gurney J. J., Erlank A. J. and Harris J.W. (1984) Origin of diamonds in old
602 enriched mantle. Nature, 310, 198- 202; doi:10.1038/310198a0.

603 Richardson, S.H., Shirey, S.B., Harris, J.W. and Carlson, R.W. (2001) Archean subduction recorded
604 by Re–Os isotopes in eclogitic sulfide inclusions in Kimberley diamonds. Earth and
605 Planetary Science Letters, 191, 257-266.

606 Rikcard, D., Griffith, A., Oldroyd, A., Butler, I.B., Lopez-Capel, E., Manning, D.A.C. and
607 Apperley, D.C. (2006) The composition of nanoparticulate mackinawite, tetragonal iron(II)
608 monosulfide. Chemical Geology, 235, 286–298.

609 Rickard, D., Mussmann, M., Steadman, J.A. (2017) Sedimentary sulphides. Elements, 13, 119-124.

610 Schoonen, M.A.A. and Barnes, H.L. (199la) Reactions forming pyrite and marcasite from solution:
611 I. Nucleation of FeS2 below 100 C. Geochimica et Cosmochimica Acta, 55 (6), 1495-1504.

612 Schoonen, M.A.A. and Barnes, H.L. (199lb) Reactions forming pyrite and marcasite from solution:
613 II. Via FeS precursors below 100 C. Geochimica et Cosmochimica Acta, 55 (6), 1505-1514.

614 Schoonen, M.A.A. and Barnes, H.L. (199lc) Mechanisms of pyrite and marcasite formation from
615 solution: III. Hydrothermal processes. Geochimica et Cosmochimica Acta 55 (12), 3491-
616 3504.

617 Seitz, H.M., Brey, G., Stachel, T. and Harris, J. (2003) Li abundances in inclusions in diamonds
618 from the upper and lower mantle. Chemical Geology, 201, 307-318.

619 Sharygin, V.V., Golovin, A.V. and Pokhilenko, N.P. Academician of the RAS Sobolev, N.V.,
620 (2003) Djerfisherite in unaltered kimberlites of the Udachnaya-East Pipe, Yakutia. Doklady
621 Earth Sciences 390, 4, 554–557.

622 Shirey, S.B., Cartigny, P., Frost, D.J., Keshav, S., Nestola, F., Nimis, P., Pearson, D.G., Sobolev,
623 N.V. and Walter, M.J. (2013) Diamonds and the geology of mantle carbon, in: Hazen, R.M.,
624 Jones, A.P., and Baross, J.A., (Eds.), Carbon in Earth: Reviews in Mineralogy &
625 Geochemistry, 75, p. 335-421.

626 Shiryaev, A.A., Frost, D.J. and Langenhorst, F. (2007) Impurity diffusion and microstructure in
627 diamonds deformed at high pressures and temperatures. Diamond and Related Materials, 16,
628 503–511.

629 Shuskanova, A.V. and Litvin, Y. A. (2008) Diamond nucleation and growth in sulfide-carbon
630 melts: an experimental study at 6.0–7.1 GPa. European Journal of Mineralogy, 20 (3), 349-
631 355.

632 Silversmidt, G., Vekemans, B., Appel, K., Schmitz, S., Schoonjans, T., Brenker, F.E., Kaminsky, F.
633 and Vincze, L. (2011) Three-Dimensional Fe Speciation of an Inclusion Cloud within an
634 Ultradeep Diamond by Confocal μ-X-ray Absorption Near Edge Structure: Evidence for
635 Late Stage Overprint. Analytical Chemistry, 83(16), 6294-9. DOI: 10.1021/ac201073s

636 Sitepu, H., Kopylova, M.G., Quirt, D.H., Cutler, J.N. and Kotzer, T.G. (2005) Synchrotron micro-
637 X-ray fluorescence analysis of natural diamonds: first steps in identification of mineral
638 inclusions in situ. American Mineralogist, 90, 1740–1747.

639 Smith, E.M., Shirey, S.B., Nestola, F., Bullock, E.S., Wang, J., Richardson, S.H. and Wang, W.
640 (2016) Large gem diamonds from metallic liquid in Earth's deep mantle. Science, 354, 1403-
641 1405.

642 Sobolev, N. V., Bartoshinskiy, Z.V., Yefimova, E.S., Lavrent'ev and Y. G. Pospelova L.N. (1970)
643 Olivine-garnet-chrome diopside assemblage from Yakutian diamond. Doklady Akademii
644 Nauk SSSR, 192, 1349-1352.

645 Sobolev, N.V. (1977) Deep-seated inclusions in kimberlites and the problem of the composition of
646 the upper mantle, American Geophysical Union, Washington, D.C., 279 p.

647 Sobolev, N. V., Fursenko, B.A., Goryainov, S.V., Shu, J., Hemley, R.J., Mao, H. and Boyd, F.R.,
648 (2000) Fossilized high pressure from the Earth's deep interior: The coesite-in-diamond
649 barometer. PNAS, 97 (22), 11875-11879. doi:10.1073/pnas.220408697.

650 Spetsius, Z.V., Belousova, E.A., Griffin, W.L., O'Reilly, S.Y. and Pearson, N.J. (2002) Archean
651 sulfide inclusions in Paleozoic zircon megacrysts from the Mir kimberlite, Yakutia:
652 implications for the dating of diamonds. Earth and Planetary Science Letters, 199, 111-126

653 Stachel, T., and Harris, J.W. (2008) The origin of cratonic diamonds - Constraints from mineral
654 inclusions. Ore Geology Reviews, 34, 5–32.

655 Stachel, T. and Luth, R.W. (2015) Diamond formation — Where, when and how? Lithos, 220–223,
656 200–220. http://dx.doi.org/10.1016/j.lithos.2015.01.028

657 Taylor, L.A. and Liu, Y. (2009) Sulfide inclusions in diamonds: not monosulfide solid solution.
658 Russian Geology and Geophysics, 50, 1201–1211.

Taylor, L., A., Logvinova, A.M., Howarth, G.H., Liu, Y., Peslier, A.H., Rossman, G.R., Guan, Y., Chen, Y. and Sobolev, N.V. (2016) Low water contents in diamond mineral inclusions: Proto-genetic origin in a dry cratonic lithosphere. Earth and Planetary Science Letters, 433, 125–132. doi.org/10.1016/j.epsl.2015.10.042.

Tempesta, G., Scandale, E. and Agrosì, G. (2011) Striations and hollow channels in rounded beryl crystals. Periodico di Mineralogia, 79/1, 75-87.

Thomassot, E. (2006) Origine et formation des diamants dans le manteau supérieur terrestre : apport d'une systématique multi-isotopique (carbone, azote et soufre). PhD thesis.

Thomassot, E., Cartigny, P., Harris J.W., Lorand J.P., Rollion-Bard C. and Chaussidon, M. (2009) Metasomatic diamond growth: A multi-isotope study (13C, 15N, 33S, 34S) of sulphide inclusions and their host diamonds from Jwaneng (Botswana). Earth and Planetary Science Letters, 282, 79–90.

Thomassot, E., Cartigny, P., Harris, J.W. and Viljoen, K.S. (2007) Methane-related diamond crystallization in the Earth's mantle: stable isotope evidences from a single diamond-bearing xenolith. Earth and Planetary Science Letters, 257, 362–371.

Titkov, S.V., Krivovichev, S.V. and Organova, N.I. (2012) Plastic deformation of natural diamonds by twinning: evidence from X-ray diffraction studies. Mineralogical Magazine, 76, 143–149.

Tkach, V.N. and Vishnevsky, A.S., 2004. Investigation of diamond single crystals of various origin using Kossel method. in ''Superhard materials. Synthesis and applications. Vol. 2, Structure and properties of superhard materials, methods of investigation'', Alkon, Kiev, 288–296.

Wang, M., Chou M., Lu, W. and De Vivo B., (2015) Effects of CH4 and CO2 on the sulfidization of goethite and magnetite: an in situ Raman spectroscopic study in high-pressure capillary optical cells at room temperature. European Journal of Mineralogy, 27, 193–201.

Wiggers de Vries, D.F., Pearson, D.G., Bulanova, G.P., Smelov, A.P., Pavlushin, A.D. and Davies, G.R. (2013) Re–Os dating of sulphide inclusions zonally distributed in single Yakutian diamonds: Evidence for multiple episodes of Proterozoic formation and protracted timescales of diamond growth. Geochimica et Cosmochimica Acta, 120, 363–394.

Westerlund, K.J., Gurney, J.J., Carlson, R.W., Shirey, S.B., Hauri, E.H. and Richardson, S.H. (2004) A metasomatic origin for late Archean eclogitic diamonds: Implications from internal morphology of diamonds and Re-Os and S isotope characteristics of their sulfide

690 inclusions from the late Jurassic Klipspringer kimberlites. South African Journal of
691 Geology, 107, 119-130, doi:10.2113/107.1-2.119.

692 Wolthers, M., Charlet, L., Van der Linde, P. R., Rickard, D. and Van der Weijden C. H. (2005)
693 Surface Chemistry of Disordered Mackinawite (FeS). Geochimica Cosmochimica Acta,
694 69(14), 3483-3492.

695 Yu, X., Raterron, P., Zhang, J., Xhijun L., Liping, W. and Zhao, Y. (2012) Constitutive Law and
696 Flow Mechanism in Diamond Deformation. Scientific Reports, 2, 876, Published online
697 2012 Nov 19. doi: 10.1038/srep00876

698

699 **Figure captions**

700 **Figure 1.** a) Optical micrograph of sample. The Miller indices of the faces are shown. b) 3D micro-
701 tomographic reconstruction of the sample. c) X-Ray traverse topograph taken using MoKα_1
702 radiation. Arrow shows the diffraction vector projection **g**. The large inclusions, with the
703 corresponding numbers in b), can be observed only in the tomographic and topographic images.
704 CP: cleavage plane. F: fracture. µL: micro-laminations.
705 **Figure 2.** X-Ray traverse topographs taken using MoKα_1 radiation. Arrows show the diffraction
706 vector projection **g**. a) and b) **g**=$2\bar{2}0$; c) and d) **g**=$\overline{311}$. µL: micro-laminations. Dashed red line
707 surrounds the core of diamond.
708 **Figure 3.** Element maps of Fe, Ni and Cu obtained by micro-XRF compared to 3D micro-
709 tomographic image of the sample, exhibiting the same orientation of the maps. CP: cleavage plane.
710 F: fracture.
711 **Figure 4.** X-Ray Diffractogram. The grey vertical lines belong to pyrrhotite (from literature), the
712 red vertical lines are the refined peak positions by HighScore Plus software, the green vertical lines
713 are pentlandite (from literature), the blue vertical lines are mackinawite (from literature). The grey
714 vertical bands indicate that with all the three phases all peaks are assigned. The most intense
715 diffraction peak of mackinawite (001) at about 5.05 Å is shown. The pie graph shows the semi-
716 quantitative mineralogical composition of the inclusions: pyrrhotite = 54%, pentlandite = 44% and
717 mackinawite = 2% (the reference codes from the ICSD database are: 98-000-5868 for pyrrhotite,
718 98-001-7595 for pentlandite and 98-004-8846 for mackinawite).
719 **Figure 5.** micro-Raman spectra. a) Comparisons among the Raman spectra of Ruff database
720 corresponding to mackinawite, pentlandite and pyrrhotite. Note the difference. b) Comparisons
721 among spectra acquired on 4 different sites of interest of the 1 inclusion and the spectrum of
722 mackinawite, ID: R060388 of Ruff database, (Lafuente et al., 2015). Note the analogy.

723

724 **Table caption**

725 **Table 1.** Mean values of the semi-quantitative analyses by micro-XRF taken on the inclusions 1, 2
726 and 3 of Figure 1b.

727

728

Figure1

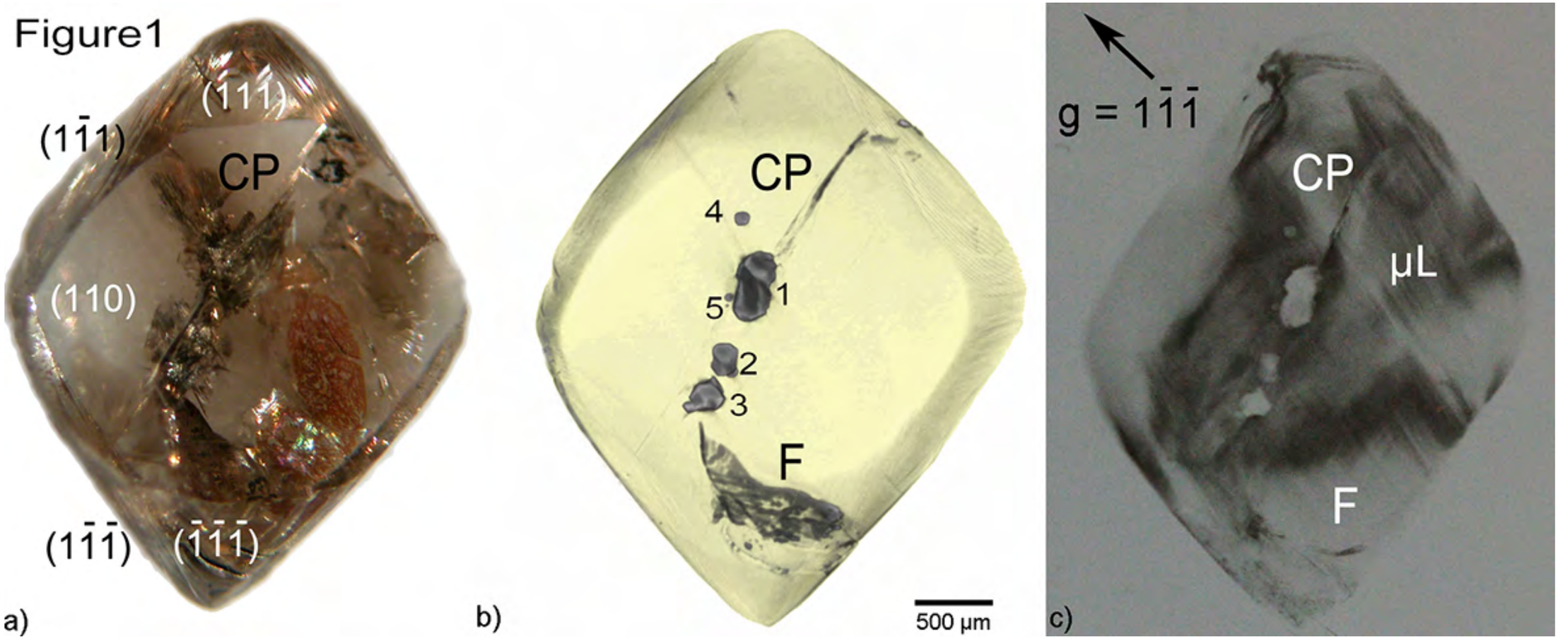

Figure 2

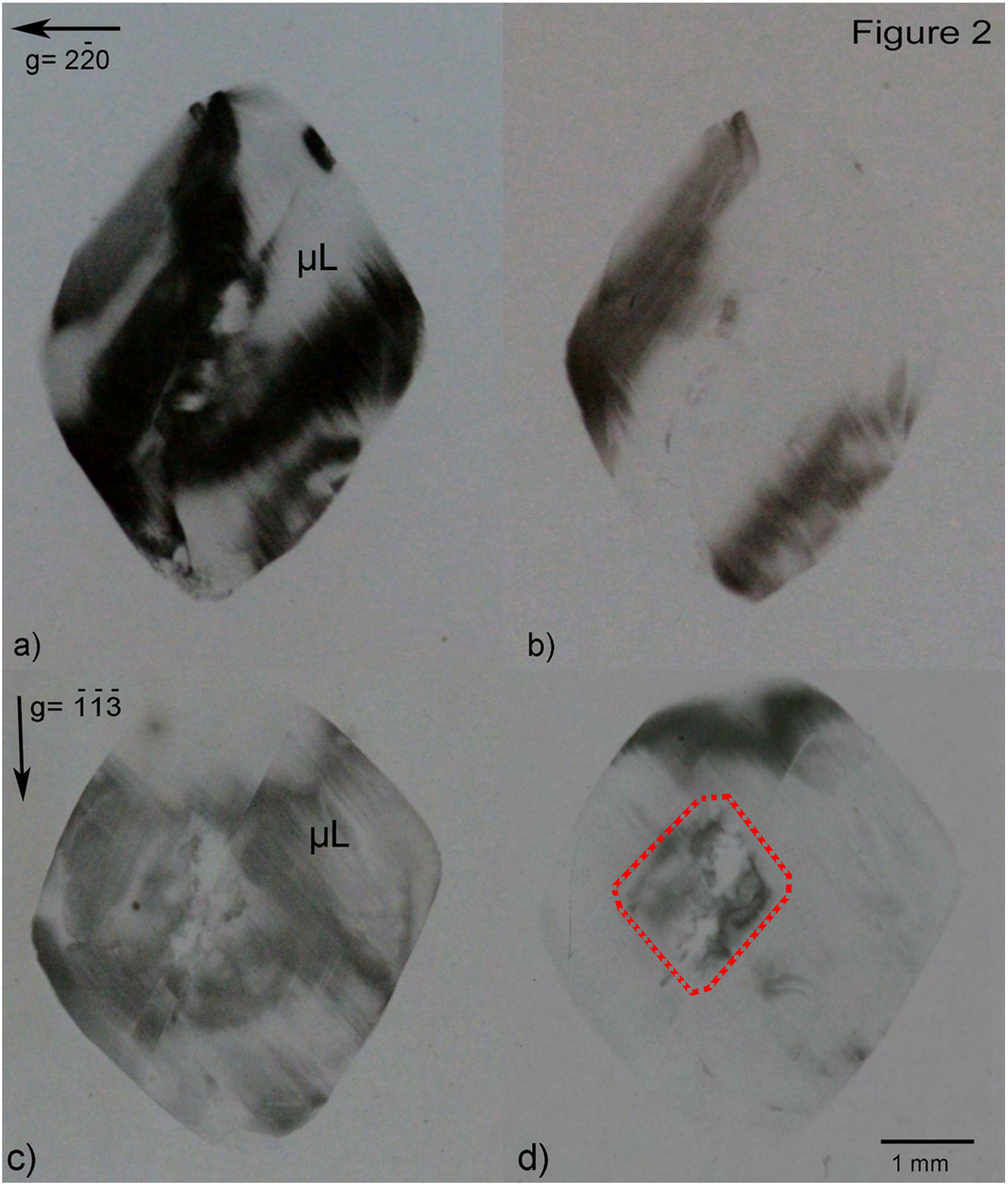

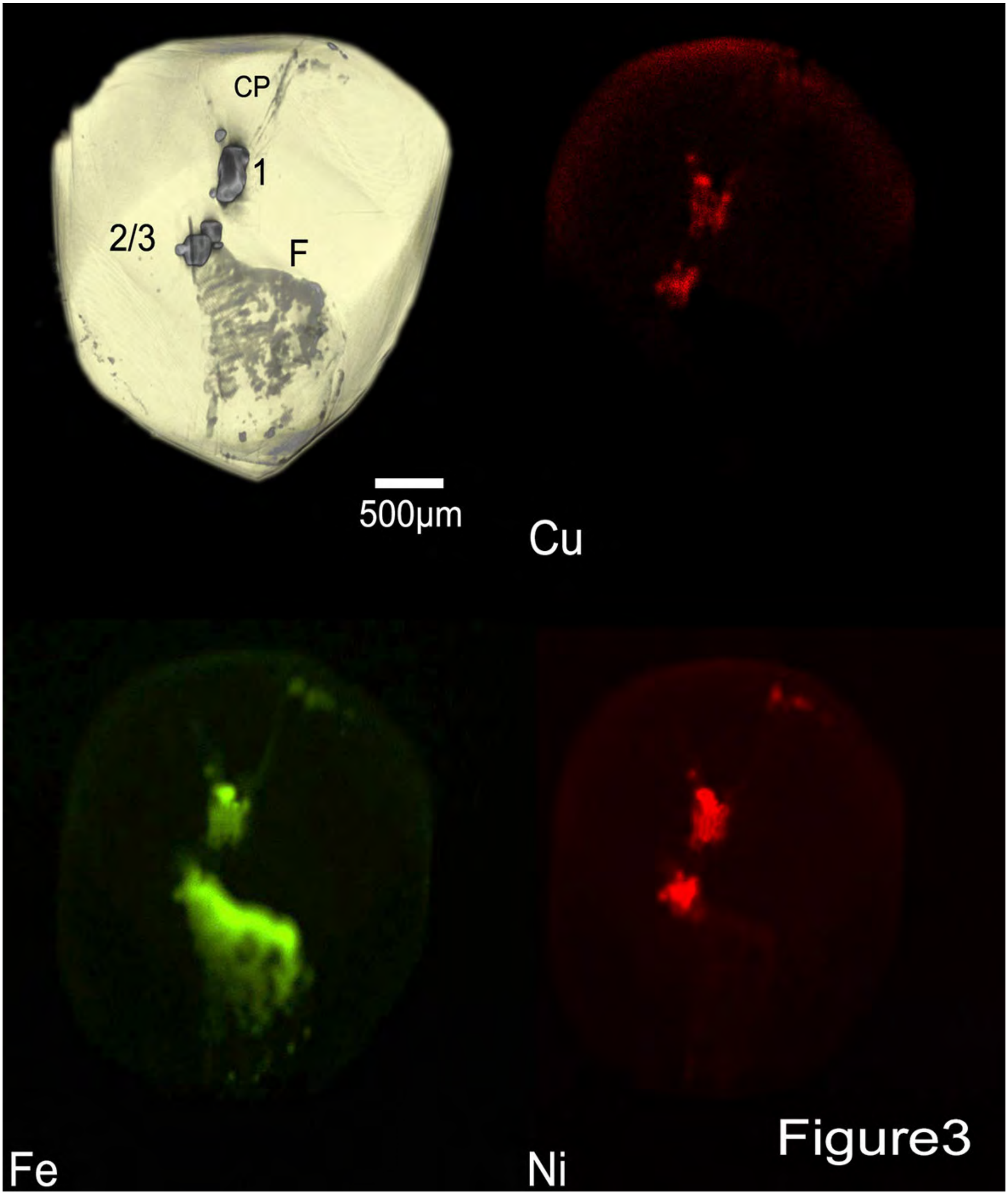
CP
1
2/3
F
500μm
Cu
Fe
Ni
Figure3

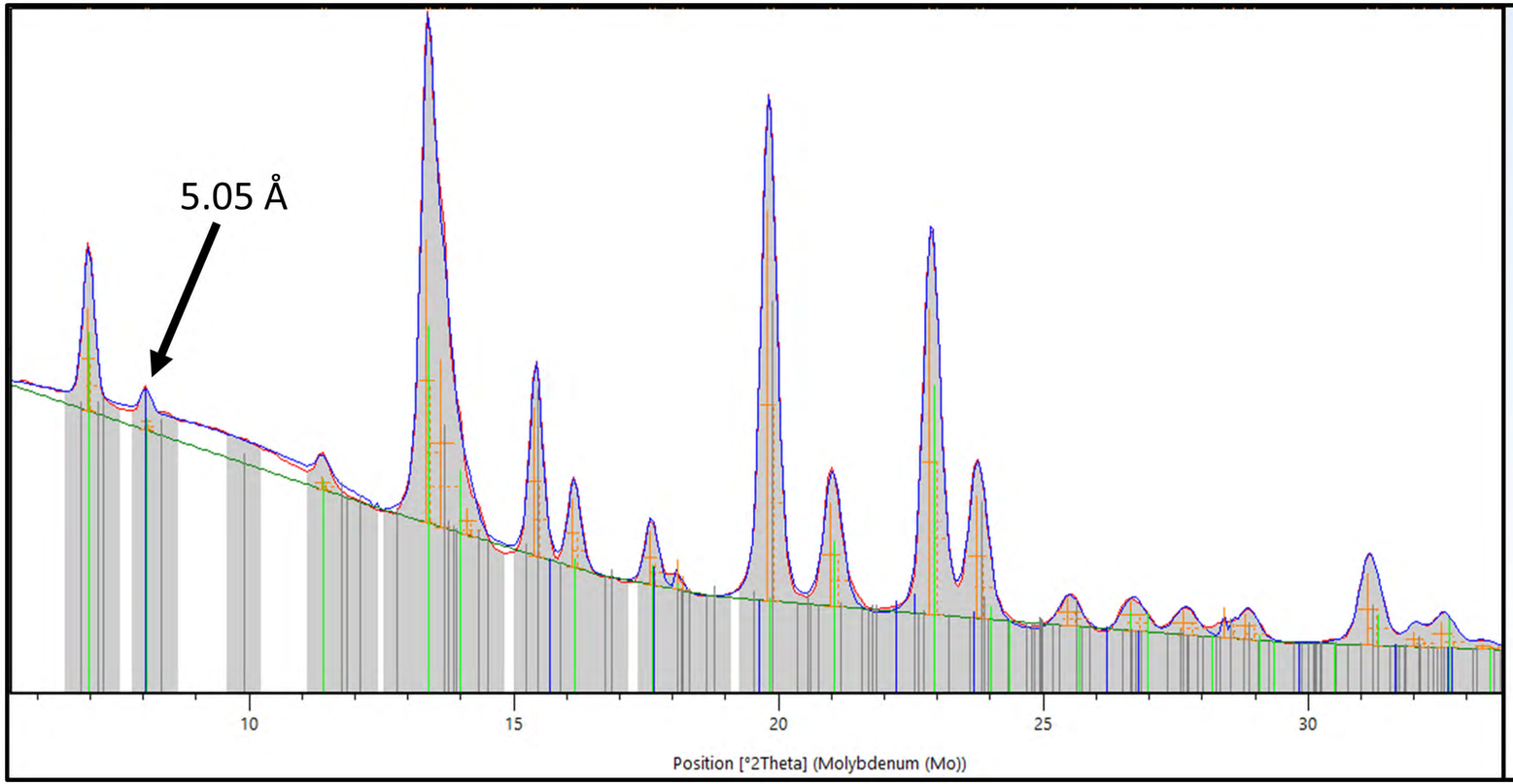
5.05 Å
10
15
20
25
30
Position [°2Theta] (Molybdenum (Mo))

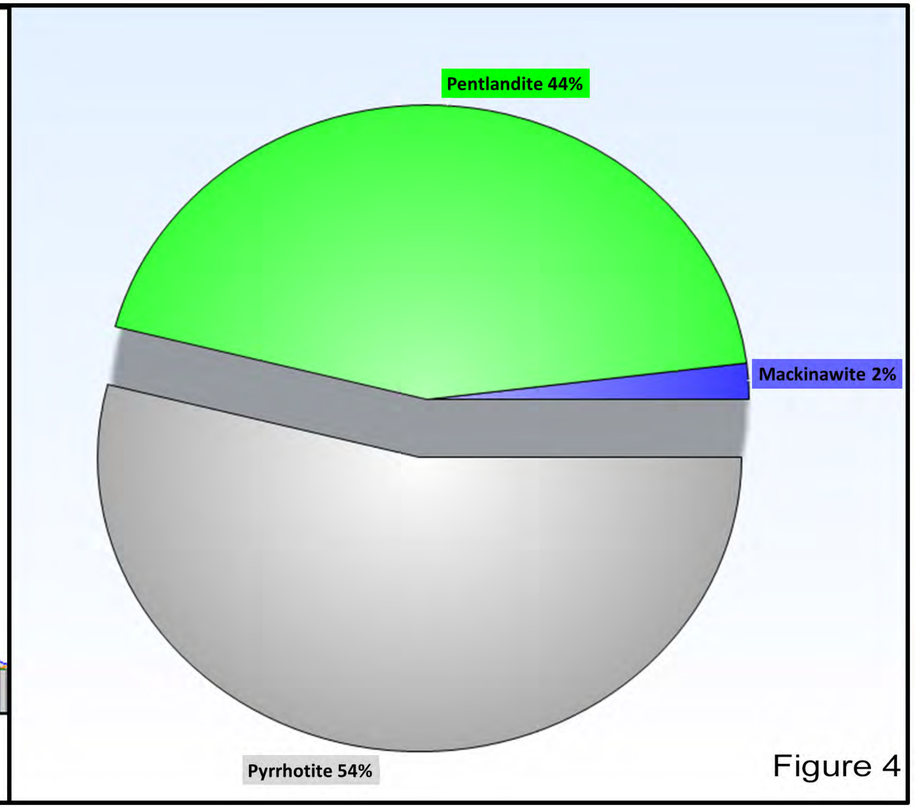
Pentlandite 44%
Mackinawite 2%
Pyrrhotite 54%

Figure 4

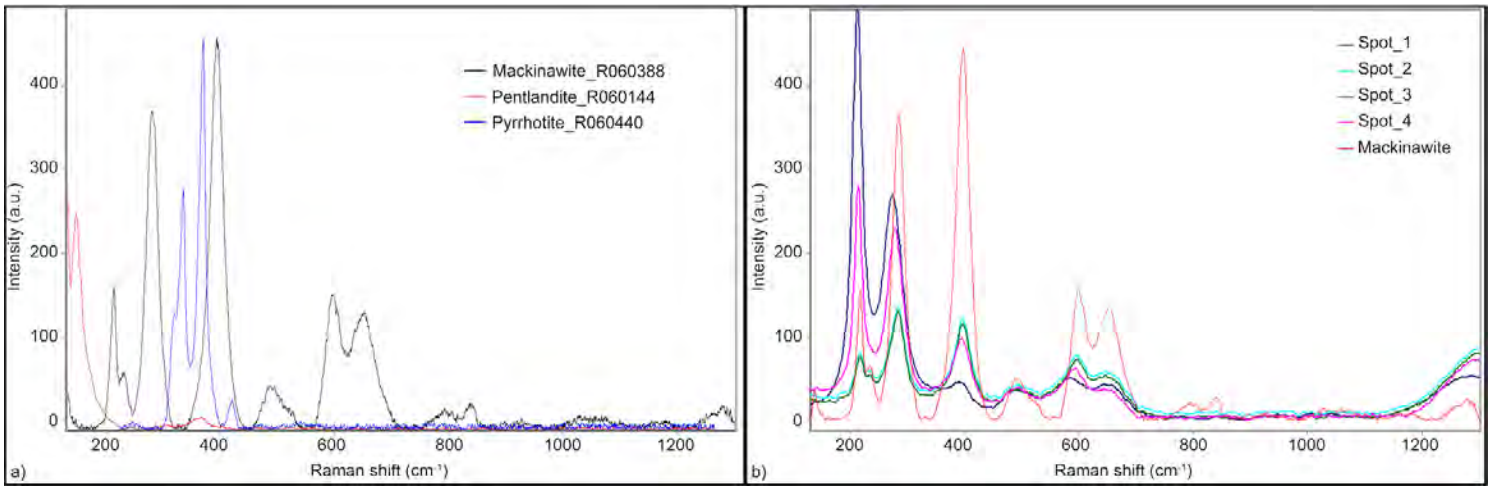
Mackinawite_R060388
Pentlandite_R060144
Pyrrhotite_R060440
Intensity (a.u.)
Raman shift (cm-1)
a)
Spot_1
Spot_2
Spot_3
Spot_4
Mackinawite
Intensity (a.u.)
Raman shift (cm-1)
b)

Table 1. Mean values of the semi- quantitative analyses by micro-XRF taken on the inclusions 1, 2 and 3.

	Incl. 1 (wt%)	Err	Incl. 2 (wt%)	Err	Incl. 3 (wt%)	Err
S	33.13	2.56	26.49	0.69	28.36	1.28
Cr	0.19	0.01	0.26	0.01	0.27	0.01
Fe	47.68	0.43	49.89	0.31	50.43	0.31
Ni	18.59	0.07	22.81	0.07	20.42	0.05
Cu	0.41	0.01	0.54	0.01	0.52	0.01